ACS APPLIED MATERIALS & INTERFACES

Research Article

www.acsami.org

Antifogging and Icing-Delay Properties of Composite Micro- and Nanostructured Surfaces

Mengxi Wen, Lei Wang, Mingqian Zhang, Lei Jiang, and Yongmei Zheng*

Key Laboratory of Bio-Inspired Smart Interfacial Science and Technology of the Ministry of Education, School of Chemistry and Environment, Beihang University, Beijing 100191, P. R. China

Supporting Information

ABSTRACT: A composite micro/nanostrucutred (MN) surface was designed using poly(vinylidene difluoride) (PVDF) polymer in combination with ZnO materials via heat-pattern-transfer and crystal-growth techniques. The surface, composed of ZnO nanohairs over PVDF microratchets (i.e., ZP-MN), displays excellent antifogging and icing-delay properties. Condensed water droplets can be easily shed from the ZP-MN surface at −5 °C for ∼1600 s via a slight wind or tilting. The droplets do not completely freeze on the ZP-MN surface at −10 °C until ∼7360 s. This investigation offers a way to design a structured surface that possesses anti-icing ability, which is significant because it can be extended to fields such as microdevices, engineering systems, and engines that operate in a cold or humid environment.

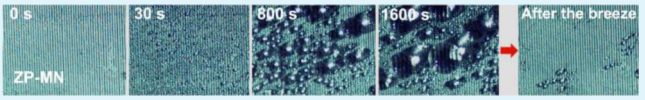

KEYWORDS: *icing delay, antifogging, micro/nanostructure, composite, wettability, low temperature*

1. INTRODUCTION

The antifogging and anti-icing abilities of a surface are significant for developing materials that can be applied in cold and humid environments.[1−11] During recent decades, many scientists have concentrated on improving the antifogging or anti-icing properties of all kinds of designed surfaces.[12−16] Until now, most of these surfaces have possessed increasingly hydrophilic or adhesive properties during or after exposure to low temperatures for long periods of time.[14,17] Improving water repellency by designing a micro- or nanostructure onto a low-surface-energy material surface, where the surface has a water contact angle (CA) greater than 150° and an extremely low sliding-off angle of no more than 10°, can result in enhanced antifoggging and anti-icing abilities.[18] Thus, the micro- and nanostructure plays a key role in the water repellency of a surface and consequently to its antifogging and anti-icing properties.[19−21] Recently, the durability of a superhydrophobic state has been investigated using a multimodal roughness texturing that is stable against mechanical stress and a 2D polymer network of fluorooxysilane chemically bound to the texture elements. The designed superhydrophobic coating can yield water contact angles exceeding 155° and a maximum rolling angle of 42° after 100 icing/deicing cycles.[1] Anti-icing ability with a long icing-delay time has been demonstrated for microperiodic-ratchet steel surfaces covered with nanohairs. In addition, the microperiodic ratchet can be used to modulate and optimize the anti-icing ability.[21] Compared with metal materials as substrates, polymer materials have lots of advantages as substrates, such as good flexibility, low cost, good adiabatic performance, and so on.[22] Polymer materials are suitable for applications in devices, for example, in a refrigerator or freezing chamber. The inner wall of the refrigerator needs certain materials that are good insulators to maintain constant temperature while minimizing outside influences (e.g., hot or cold surrounding temperature, etc.). Some research has been conducted on dropwise condensation and frosting suppression on hierarchical surfaces.[23,24] However, little investigation examining both antifogging and anti-icing together on a polymer surface composed of designed micro- and nanostructures has been reported.

In this study, a composite micro/nanostrucutre surface was designed using poly(vinylidene difluoride) (PVDF) polymer in combination with zinc oxide (ZnO) materials to realize a ZnO-on-PVDF micro/nanostructure (ZP-MN). In this fabrication, a heat-pressing pattern-template method was adopted to obtain a microratchet PVDF polymer surface as the substrate. Then, ZnO nanohairs were planted onto the microratchet PVDF polymer substrate. Lastly, the antifogging and anti-icing properties of the ZP-MN surface were examined at low temperatures of −5 or −10 °C. This investigation is significant because it offers insight into a composite micro/nanostructure surface as well as a way to design a structured surface with anti-icing ability, which is significant because it can be extended to fields such as microdevices, engineering systems, and engines that operate in a cold or humid environment.

2. EXPERIMENTAL SECTION

Preparation of the ZP-MN Surfaces. First, the crystal seed was prepared as follows: 2.195 g of $Zn(Ac)_2{\cdot}2H_2O$ (SCRC, A.R.), 20 mL of ethylene glycol-monomethyl ether (SCRS, A.R.), and 0.6108 g of monoethanolamine (Beijng Chemical Plant, A.R.) were mixed and then stirred for ∼30 min to dissolve the mixture completely. The crystalline powder was mixed with organic powder (poly(vinylidene difluoride), PVDF, MW = 530 000, Aldrich) in a ratio of 1:100. Second, the surface of a stainless steel plate was machined to form the

Received: November 20, 2013
Accepted: February 26, 2014
Published: February 26, 2014

   dx.doi.org/10.1021/am405232e | ACS Appl. Mater. Interfaces 2014, 6, 3963−3968

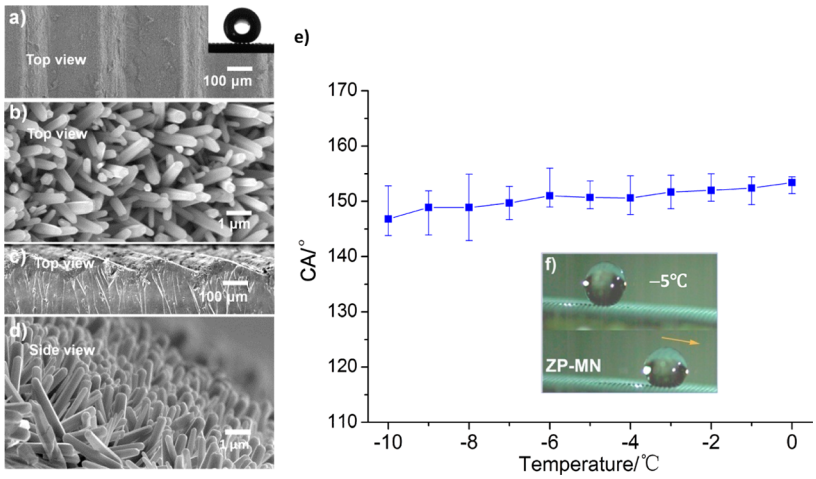

Figure 1. (a–d) SEM images of the ZP-MN surface: top view (a, b) and side view (c, d). The microratchets are ~300 μm in periodicity (a) and ~70 μm in height (c). The ZnO nanohairs are ~300–500 nm in diameter (b) and ~2 to 3 μm in height (d). (e) Relationship between the contact angles (CAs) on the surfaces versus temperature. The CAs change from ~160.2 to ~146.8° at the temperature is decreased from 0 to −10 °C. (f) Optical image of the droplet rolling-off process on a ZP-MN surface at −5 °C; the droplet rolling-off angle is ~5°.

micrometer-scale ratchet structure with a periodicity of ~300 μm and a ratchet height of ~70 μm. The crystalline–organic powder mixture was then placed on glass, and the glass was placed on a heating plate with the temperature of ~260–300 °C. Subsequently, when the mixture powder was melted at ~270 °C, the microratchet stainless steel plate as the template was placed on the powder mixture, and then a pressing force of ~100 N was exerted on the microratchet stainless steel plate for ~30 s to promote close contact with the melted mixture powder. The sheet glass was removed from the heating plate together with the microratchet stainless steel plate until they cooled. Next, the sheet glass and microratchet stainless plate were separated from each other, from which the solidified microratchet polymer surface remained. After this, we cut the organic plates (PVDF) into a rectangular surface of ~30.0 mm in length, ~10.0 mm in width, and ~1.0 mm in height. Third, the ZnO nanohairs were planted on the polymer surface with microratchets by a crystal growth method. Thus, the composite surfaces composed of PVDF microratchet and ZnO nanohairs (i.e., ZP-MN) were fabricated successfully. The ZP-MN surfaces were placed upright into an agitating Teflon reactor, and the mother liquor was poured into the reactor. Mother liquor was prepared as follows: 0.7436 g of $Zn(NO_3)_2{\cdot}6H_2O$ (SCRS, A.R.) and 0.3505 g of hexamethylenetetramine (Beijing YiLi Fine Chemicals Co., LTD, A.R.) were mixed into 100 mL of deionized water and stirred for ~30 min. Then, the agitated reactor was placed into an oven at ~90 °C for ~20 h. After the reaction was completed, the surface was washed with deionized water and then dried in an oven. The surfaces were plasma-cleaned (PDC-32G, Harrick Plasma) at high power for ~10 min to enhance their chemical activity. Then, the surfaces were placed into a vacuum dryer, and two droplets of heptadecafluorodecyltripropoxysilane (FAS-17) was injected in the dryer. The vacuum dryer was placed under reduced pressure at −0.1 MPa and kept in an oven at ~60 °C for ~12 h without light. In this way, the ZP-MN surfaces were of low surface energy. By this method above, a nanostrucutre (N) surface, microstructure (M) surface, and smooth (S) surface were be obtained. After being modified by FAS-17, all surfaces had the same hydrophobic group monolayer for performing control experiments.

Measurement of Static/Dynamic Water Contact Angles. Water contact angles (CAs) were tested using an optical contact-angle meter system with a cooling stage controller (Dataphysics SCA40, Germany) at different temperatures. The temperature of the cooling stage could be controlled from −10 to 30 °C, and the samples were fixed on the cooling stage using copper foil double-sided conductive tape. Droplets (7 μL in volume, pure water) were placed gently onto the surfaces. An optical contact-angle system was used to test the CAs. The advancing contact angles (ACAs) and receding contact angles (RCAs) were tested in which the droplets were enlarged from 7 to 14 μL to obtain ACAs and shrunk from 14 to 7 μL to obtain RCAs. The sliding-off angles were measured by sloping the surface at −5 °C. The ambient temperature and relative humidity were ~20.8 ± 3 °C and ~26.7 ± 10%, respectively.

Observation of Droplet Condensation. The surface was placed on a cooling stage, which could maintain its temperature at −5 °C. The temperature of the surfaces was inspected using a digital temperature sensor. After ~60 s, the spray of a humidifier was used to generate condensed water droplets on the surface. After the surfaces were sprayed (~1600 s), a gentle breeze (wind speed of ~1 m s^{-1}) was directed toward the surfaces. At the same time, the dynamic process of the condensed droplet's growth was recorded by the optical contact-angle meter system with a cooling stage controller (Dataphysics SCA40, Germany). The condensation experiments were repeated for several times. The room temperature and relative humidity were ~25.8 ± 2 °C and ~30.6 ± 10%, respectively.

Measurement of the Sliding-Off Angles. The surfaces were fixed using copper foil double-sided conductive tape to the cooling stage that controlled the surface's temperature at −5 °C. The temperature of the surfaces was inspected using a digital temperature sensor. After ~60 s, 7 μL droplets were placed on the surfaces. Subsequently, the surfaces together with the cooling stage were tilted slowly until the droplets rolled away from the surfaces. This dynamic process of droplet rolling-off was recorded by a high-speed camera. The slidding-off angles of the droplets were measured using a contact-angle meter (Dataphysics SCA40, Germany).

Delay Time Experiment. The surfaces were fixed using copper foil double-sided conductive tape onto the cooling stage that controlled the surface's temperature at −10 °C. The temperature of the surfaces was inspected using a digital temperature sensor. Then, 7 μL droplets were placed onto the surfaces. The freezing process of the droplets was recorded using a CCD camera. The delay times were determined by recording the time at which the droplets changed from transparent to nontransparent (i.e., droplet freezing). The room temperature and relative humidity were ~23.8 ± 2 °C and ~50.6 ± 10%, respectively.

Test of the Wind Force to Blow Away the Droplet. The surfaces were fixed using copper foil double-sided conductive tape onto the cooling stage that controlled surface's temperature at −10 °C. The temperature of the surfaces was inspected using a digital temperature sensor. Then, 7 μL droplets were deposited on the surfaces. Wind was used to blow the droplets on the surfaces with different delay times. The minimum wind speed was estimated, and the force of the wind was estimated quantitatively by directing the

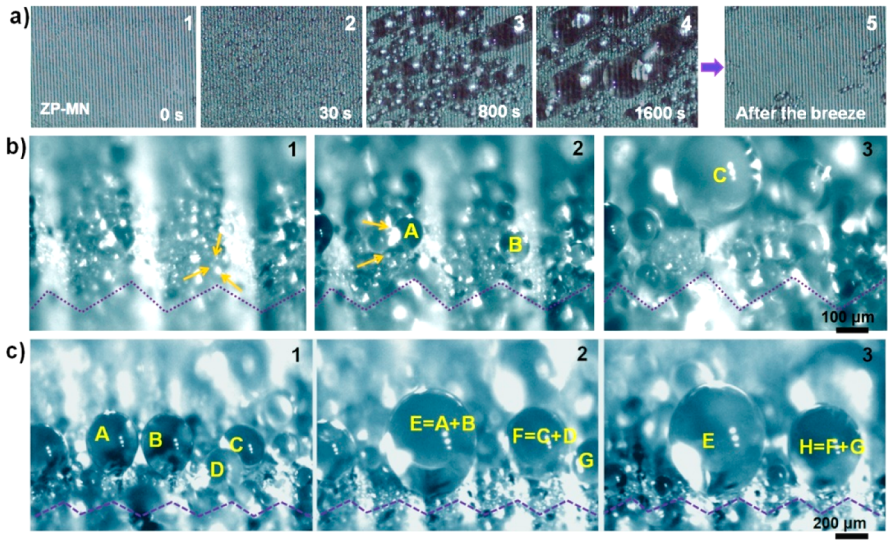

Figure 2. Optical images of the antifogging properties of the ZP-MN surface. The surfaces were maintained at a temperature of −5 °C. The room temperature was ∼25.8 ± 2 °C, and the relative humidity was ∼30.6 ± 10%. (a) Droplet shedding-off property of the ZP-MN surface. The condensed droplets were formed on ZP-MN over 0−1600 s (frames 1−4). The droplets formed on the ZP-MN surface after ∼1600 s are shed by the applied breeze (from 5). (b) Magnified high-resolution images captured with a CCD camera. The tiny droplets initially condense on the nanohair (frame 1). These tiny droplets grow in size and then merge with each other onto the top of the microratchet along the vertical direction (e.g., they form droplet A and B; frame 2). With passing time, the other tiny droplets will merge with A and form droplet C, with a diameter of ∼150 μm (frame 3). (c) Magnified low-resolution images of the interface. As the droplets (A−D) grow larger, with a diameter of more than ∼150 μm (frame 1), they will merge with each other along the horizontal direction. Droplets A and B coalesce into larger droplet E; C and D coalesce into larger droplet F (frame 2). Then, droplet G merges with droplet F and forms droplet H (frame 3).

wind toward an electronic balance. Thus, the relationship between the delay times and the wind force was determined.

Observation of Condensed Droplet Shedding. The cooling stage was tilted to an angle of 60°, and a humidifier was used to spray droplets onto the surfaces. The dyanmic process of droplet coalescence was recorded using a CCD camera. The room temperature and relative humidity were ∼23.6 ± 3 °C and ∼28.4 ± 10%, respectively.

3. RESULTS AND DISCUSSION

A composite PVDF power mixture including a crystalline seed was prepared (see Experimental Section). The composite PVDF microstructure (M) polymer surface was fabricated by a heat-pressing technique via a metal template with a microratchet array (illustrated in Supporting Information Figure S1a). Then, ZnO nanohairs were planted on the PVDF polymer surface by controlling crystal growth.[25−30] By this process, the composite micro- and nanostructured surface composed of microratchet PVDF and ZnO nanohairs (i.e., ZP-MN surface) was fabricated successfully. Figure 1a−d shows scanning electron microscopy (SEM) images of the ZP-MN surface from the top and side views. The microratchets are ∼300 μm in periodicity and ∼70 μm in height (Figure 1a,c). The nanohairs completely cover the microratchet and have a diameter of ∼300−500 nm and height of ∼2 to 3 μm (Figure 1b,d); these features are considered to favor the anti-icing ability of the composite because of the high ratio of trapped air.[31] The inset shows an optical image of a droplet (7 μL) on the ZP-MN surface under ambient conditions. Using this method, other surfaces, such as the N , M , and S surfaces (see Supporting Information Figure S1b), were obtained for use in control experiments to investigate the antifogging and icing-delay properties of the composite.

The wetting properties of these surfaces were examined by measurement of water contact angles (CAs) via an optical contact-angle system. The surfaces were controlled to temperatures from 0 to −10 °C. The ambient temperature and relative humidity were ∼20.8 ± 3 °C and ∼26.7 ± 10%, respectively. Figure 1e shows the CAs of the ZP-MN surface over the temperature range from 0 to −10 °C, where the CAs change little with the decreasing temperature (i.e., from 160.2° at 0 °C to 146.8° at −10 °C). In addition, ZP-MN has a low rolling-off angle of ∼5° for a 7 μL droplet (Figure 1f and see Supporting Information Figure S2). This indicates that at low temperature the ZP-MN surface is kept in an excellent superhydrophobic state in which the nanohairs and the microstructure may be improving the low-temperature hydrophobic property of surface.[32]

The low-temperature superhydrophobic property was elucidated by the Cassie−Baxter model,[33] indicating that the microstructure on a low-surface-energy material signficantly improves the superhydrophobicity of the surface. The effective CA of the droplets can be regulated by the equation $\cos\theta^* = f_A \cos\theta_A + f_B \cos\theta_B$, where $f_{A,B}$ are the surface area fractions of the components and $\theta_{A,B}$ are the Young contact angles of the components. If rough structures on a surface can generate entrapped air pockets, then the effective CA will considerably increase.[34] Because the θ_B of the air is 180°, this relationship is followed as

$$\cos\theta^* = f_A(\cos\theta_A + 1) - 1 \quad (1)$$

In this case, the capability of capturing air pockets is an important property for the low-temperature superhydrophobicity of a surface. The nanohairs array traps the air in its interspaces, which allows the MN surface to have a high CA. The high aspect ratio of the nanohairs on the surface drastically reduces the contact area of a droplet with the surface (i.e., a smaller area fraction, f_A, is obtained, which results in a high-

suspended spherical droplet for low-temperature water repellency).

Antifogging property was also examined on the ZP-MN surface. We placed the ZP-MN surface on a cooling stage to maintain a low temperature of −5 °C. The room temperature and relative humidity were ∼25.8 ± 2 °C and ∼30.6 ± 10%, respectively. After 60 s, a humidity of 90% was applied onto the ZP-MN surface using a humidifier, and the performance of the condensed water droplets was recorded using a CCD camera. As shown in Figure 2a, condensed water droplets are observed on the ZP-MN surface at −5 °C over 0−1600 s (frames 1−4). The surface makes the condensed water droplets gather into a large one by ∼1600 s (frame 4). When we used a gentle breeze (wind speed of ∼0.5 m s^{-1}) to blow onto the surfaces, the droplets on the surface were easily blown away and almost completely removed (frame 5), which is a better performance than other surfaces (e.g., the N, M, and S surfaces (see Supporting Information Figure S3). This experiment was repeated many times, and the droplets were always easily blown from the ZP-MN surface (see Supporting Information Figure S4). Therefore, the ZP-MN surface displays an excellent antifogging property.

To examine the antifogging property further, we explored the merging of tiny condensed droplets on the micro/nanostructure surface. As shown in Figure 2b, at the beginning (frame 1), the tiny droplets condense on the top of the nanohair because of the nanopockets (see arrows). Then, some tiny droplets merge with each other along the vertical direction and form droplets A and B (frame 2). With passing time, the other tiny droplets will merge with A and form droplet C (frame 3). We found that when the diameter of the droplet is less than 150 μm (see Supporting Information Figure S5), the tiny droplets merge with each other along the vertical direction, and when the diameter of the droplets is larger than 150 μm, they will easily merge with each other along the horizontal direction. As shown in Figure 2c, droplets A−D are growing (frame 1). Subsequently, droplets A and B coalesce into larger droplet E; C and D coalesce into larger droplet F (frame 2). Then, droplet G merges with droplet F and forms droplet H (frame 3). This indicates that the condensed droplets can be in Cassie's state after droplet merging on the micro- and nanostructure.

Furthermore, the ZP-MN surface was tilted to 60° and maintained at −5 °C, the fog spray was applied to the surfaces, and the dynamic process of droplet movement was recorded using a CCD camera. As shown in Figure 3a, some tiny droplets initially condensed on the surface and subsequently the droplets grew to a certain size (e.g., ∼150−500 μm) (frame 1). These droplets roll off easily (frame 2). It is interesting that this roll-off performance removes some tiny droplets (frame 3), sweeping the surface clean (frame 4), where the dry area remains (see yellow circle in frames 2−4). To assess the antifogging ability of the ZP-MN surface, we evaluated the proportion of area versus time (Figure 3b). At ∼100 s, the proportion is lower, but the proportion increases slowly after ∼300 s. The proportion can be basically maintained at ∼80% from ∼300 to 1000 s. This demonstrates the excellent antifogging property of the ZP-MN surface.

To demonstrate the anti-icing ability of the ZP-MN surface, the surfaces were placed in a cooling stage with a temperature of −10 °C. A ∼7 μL droplet was deposited on the surface as a reference droplet that is used to observe how long the droplet is maintained before freezing. The delay time for the droplets to freeze on the surfaces at −10 °C was recorded by observing the

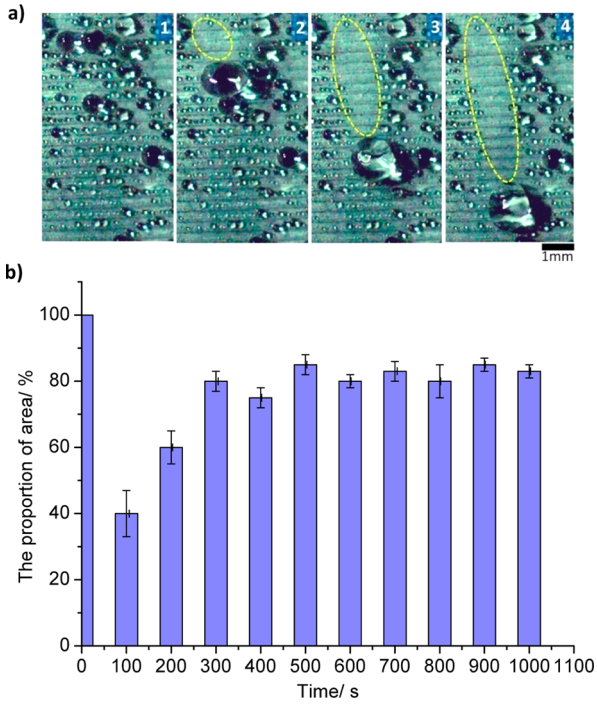

Figure 3. Defogging ability of the ZP-MN surface. (a) Optical images showing tiny droplets rolling away from the ZP-MN surface. From frames 1−4, with water condensation, the droplets grow (frame 1). As the droplets reach a certain size (e.g., ∼150−500 μm), the droplets will roll away easily (frame 2). Additionally, the grown droplets also sweep away some tiny droplets (frames 3 to 4) and the area remains dry (yellow circle in frames 2−4). (b) Statistics of the relationship between the proportion of area versus time. At ∼100 s, the proportion is lower, but the proportion increases slowly after ∼300 s. The proportion can be basically maintained at ∼80% from ∼300 to 1000 s.

transparency of the droplet. Figure 4a shows statistics on the icing-delay time of the four surfaces. The droplet on the M surface was frozen first (∼300 ± 20 s). The droplets on the S and N surfaces froze next (∼720 ± 32 and ∼2280 ± 60 s, respectively). In contrast, the droplet on the ZP-MN surface did not freeze by ∼6360 ± 120 s. The droplet does not completely freeze on the MN surface until ∼7360 s, demonstrating its long icing-delay time that is superior to the other surfaces. The inset shows the optical images of the in situ observation of four surfaces on which the droplets were frozen over time.

To determine the extent of droplet adhesion on the ZP-MN surface under low temperature over time, we examined droplets shedding off of the ZP-MN surface at low temperature over time. Figure 4b shows the relationship between the delay time and the wind force to blow away the droplet (7 μL) on the ZP-MN surface at −10 °C. The wind force was increased from ∼1 to ∼6 μN to blow away the droplets on the surface with delay time from 0 to ∼7000 s. At the beginning, a force of 1 μN can blow away the droplets from the surface easily. When the droplets are about to freeze, the wind froce that blows away the droplets needs to be stronger, up to ∼6 μN. So, the droplets are blown away easily before the droplets are frozen. This indicates the excellent anti-icing ability of ZP-MN surface at below-zero temperatures. Under normal conditions, as illustrated in Supporting Information Figure S6, when the droplet is suspended on the ZP-MN surface, the small droplets will be generated on the nanostructure below. With passing time, the

dx.doi.org/10.1021/am405232e | ACS Appl. Mater. Interfaces 2014, 6, 3963−3968

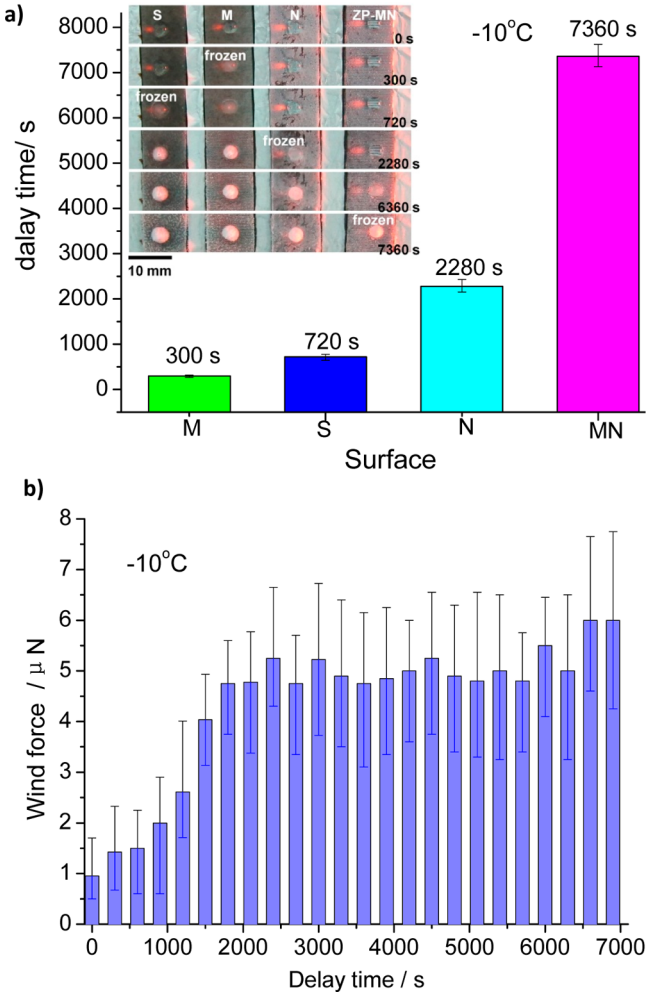

Figure 4. (a) Droplets freezing and icing-delay time of the four surfaces at −10 °C. The transparent droplets (7 μL) become nontransparent on the M, S, N, and ZP-MN surfacesafter ∼300 ± 20, ∼720 ± 32, ∼2280 ± 60, and ∼6360 ± 120 s, respectively. The longest delay time is ∼7360 s on the ZP-MN surface. The inset shows images of droplets frozen on these surfaces. (b) Relationship of the delay time versus wind force to blow away the droplets on the ZP-MN surface at −10 °C. At the beginning, a force of ∼1 μN can blow away the droplets from the ZP-MN surface easily. The wind force is less than 5 μN at a delay time of ∼1500−6000 s. The wind force reaches ∼6 μN at a delay time of ∼7000 s.

little droplet grows bigger. When it increases to a certain extent, it will merge with the large droplet because of the low surface energy of the nanostructure. So, the attraction force of the large droplet is stronger than the adhension of the small droplet. Under this condition, a droplet on the ZP-MN surface can maintain a Cassie state. Although the droplet stays on the surface for a long time, it still has a small three-phase contact line. This can explain why the droplets that remain on the surface even after a very long time can be easily blown away.

As for the anti-icing ability of the ZP-MN surface, we consider the droplet on the surface as a system of solid−liquid−air three-phase interfaces. In a low-temperature environment, the droplet loses heat to the cold surface through contact heat conduction and thermal radiation between the droplet and the structure. At the same time, it gains heat from air in the form of contact heat conduction and thermal radiation. The heat that the droplet loses per unit time can be expressed as $\Delta h = h_1 + h_{1'} - h_g - h_{g'}$, where Δh is the net heat loss in unit time ($\Delta h > 0$ means that the surface is in a low-temperature environment), h_1 and $h_{1'}$ are heat loss through contact heat conduction and thermal radiation to the surface per unit time, respectively, and h_g and $h_{g'}$ are heat gains through contact heat conduction and thermal radiation per unit time from the air, respectively. In this case, the time for the droplets to be frozen completely at a certain temperature can be expressed as[21]

$$\Delta t \propto \frac{\rho_w C_p (T_0 - T_s)}{\Delta h} \quad (2)$$

where Δt is the freezing time of the droplet at certain temperature (i.e., the delay time that it takes for the droplet to be frozen completely), ρ_w is the water density, C_p is the heat capacity of pure water at constant pressure, T_0 is the initial temperature of the droplet, and T_s is the sample surface temperature. This indicates that Δt is in inverse proportion to Δh (i.e., the larger Δt, the smaller Δh must be). To combine the solid−liquid−air interface effect, the ZP-MN surface forms the lowest liquid−solid contact area because of the cooperative effect of the micro- and nanostructure followed by the N, S, and M surfaces, respectively. In our experiment, the M surface forms the highest liquid−solid contact area instead of that of S surface, which is inferred from droplet's reduced ability to slide off (see Figure S2 and illustrated in Figure S7c) and may be a result of this surface's long microscale periodicity. From the surface to the droplet, the lower liquid−solid contact area would induce the larger liquid−air contact area; thus, less heat would be lost through contact heat conduction and thermal radiation to the surface. Further inferred from eq 2, the ZP-MN surface to the droplet forms the smallest Δh because of the larger liquid−air contact area, whereas the M surface to the droplet forms the lowest liquid−air contact area in this study. The N and S surfaces are intermediate (see Supporting Information). Thus, the droplet's freezing has the longest delay time, Δt, on the ZP-MN surfaces.

4. CONCLUSIONS

We have designed an excellent antifogging/anti-icing polymer surface (ZP-MN) with a microstructure that is composed of PVDF and a nanostructure composed of ZnO. The effect of the micro- and nanostructure is that it induces tiny condensed droplets to merge with each other easily and then shed from the ZP-MN surface, where the surface remains dry. This investigation opens insights into designing structured polymer surface materials to realize antifogging, anti-icing, or antifrosting capabilities that can be applied into microdevices used in cold, damp environments.

■ ASSOCIATED CONTENT

Supporting Information

Preparation process of the microstructure; SEM images of the M, N, and S structure's surface; measurement of the sliding-off angles on the four surfaces; images of water condensation; and analysis of the model for the heat-transfer process. This material is available free of charge via the Internet at http://pubs.acs.org.

■ AUTHOR INFORMATION

Corresponding Author

*E-mail:zhengym@buaa.edu.cn.

Notes

The authors declare no competing financial interest.

■ ACKNOWLEDGMENTS

This study was supported by the National Natural Science Foundation of China (21234001), National Research Fund for Fundamental Key Project (2013CB933000), Doctoral Fund of the Ministry of Education of China (20121102110035), and Graduate Student Innovation Practice Foundation of Beihang University.

■ REFERENCES

(1) Boinovich, L. B.; Emelyanenko, A. M.; Ivanov, V. K.; Pashinin, A. S. Durable Icephobic Coating for Stainless Steel. *ACS Appl. Mater. Interfaces* **2013**, *5*, 2549−2554.
(2) Erbil, H. Y.; Demirel, A. L.; Avcı, Y.; Mert, O. Transformation of a Simple Plastic into a Superhydrophobic Surface. *Science* **2003**, *299*, 1377−1380.
(3) Sun, T.; Feng, L.; Gao, X.; Jiang, L. Bioinspired Surfaces with Special Wettability. *Acc. Chem. Res.* **2005**, *38*, 644−652.
(4) Boinovich, L. B.; Emelyanenko, A. M. Anti-icing Potential of Superhydrophobic Coatings. *Mendeleev Commun.* **2013**, *23*, 3−10.
(5) Hejazi, V.; Sobolev, K.; Nosonovsky, M. From Superhydrophobicity to Icephobicity: Forces and Interaction Analysis. *Sci. Rep.* **2013**, *3*, 2194-1−2194-6.
(6) Park, S.-H.; Cho, E.-H.; Sohn, J.; Theilmann, P.; Chu, K.; Lee, S.; Sohn, Y.; Kim, D.; Kim, B. Design of Multi-Functional Dual Hole Patterned Carbon Nanotube Composites with Superhydrophobicity and Durability. *Nano Res.* **2013**, *6*, 389−398.
(7) Liu, M.; Zheng, Y.; Zhai, J.; Jiang, L. Bioinspired Super-Antiwetting Interfaces with Special Liquid−Solid Adhesion. *Acc. Chem. Res.* **2009**, *43*, 368−377.
(8) Zheng, Y.; Bai, H.; Huang, Z.; Tian, X.; Nie, F.-Q.; Zhao, Y.; Zhai, J.; Jiang, L. Directional Water Collection on Wetted Spider Silk. *Nature* **2010**, *463*, 640−643.
(9) Feng, L.; Li, S.; Li, Y.; Li, H.; Zhang, L.; Zhai, J.; Song, Y.; Liu, B.; Jiang, L.; Zhu, D. Super-Hydrophobic Surfaces: From Natural to Artificial. *Adv. Mater.* **2002**, *14*, 1857−1860.
(10) Hancock, M. J.; Sekeroglu, K.; Demirel, M. C. Bioinspired Directional Surfaces for Adhesion, Wetting, and Transport. *Adv. Funct. Mater.* **2012**, *22*, 2223−2234.
(11) Asmatulu, R.; Ceylan, M.; Nuraje, N. Study of Superhydrophobic Electrospun Nanocomposite Fibers for Energy Systems. *Langmuir* **2010**, *27*, 504−507.
(12) Chevallier, P.; Turgeon, S. P.; Sarra-Bournet, C.; Turcotte, R.; Laroche, G. T. Characterization of Multilayer Anti-Fog Coatings. *ACS Appl. Mater. Interfaces* **2011**, *3*, 750−758.
(13) Maechler, L.; Sarra-Bournet, C.; Chevallier, P.; Gherardi, N.; Laroche, G. Anti-Fog Layer Deposition onto Polymer Materials: A Multi-Step Approach. *Plasma Chem. Plasma Process.* **2011**, *31*, 175−187.
(14) Tricoli, A.; Righettoni, M.; Pratsinis, S. E. Anti-Fogging Nanofibrous SiO_2 and Nanostructured SiO_2−TiO_2 Films Made by Rapid Flame Deposition and in Situ Annealing. *Langmuir* **2009**, *25*, 12578−12584.
(15) Jia, Y.; Liu, G.; Wu, X.; Liu, H.; Yue, R.; Chen, Y. Anti-Fogging and Anti-Reflective Silica Nanofibrous Film Fabricated by Seedless Flame Method. *Mater. Lett.* **2013**, *108*, 200−203.
(16) McDonald, B. T.; Cui, T. Superhydrophilic Surface Modification of Copper Surfaces by Layer-by-Layer Self-Assembly and Liquid Phase Deposition of TiO_2 Thin Film. *J. Colloid Interface Sci.* **2011**, *354*, 1−6.
(17) Howarter, J. A.; Youngblood, J. P. Self-Cleaning and Next Generation Anti-Fog Surfaces and Coatings. *Macromol. Rapid Commun.* **2008**, *29*, 455−466.
(18) Cebeci, F. Ç.; Wu, Z.; Zhai, L.; Cohen, R. E.; Rubner, M. F. Nanoporosity-Driven Superhydrophilicity: A Means To Create Multifunctional Antifogging Coatings. *Langmuir* **2006**, *22*, 2856−2862.
(19) Guo, P.; Zheng, Y.; Liu, C.; Ju, J.; Jiang, L. Directional Shedding-Off of Water on Natural/Bio-Mimetic Taper-Ratchet Array Surfaces. *Soft Matter* **2012**, *8*, 1770−1775.
(20) Shirtcliffe, N. J.; McHale, G.; Newton, M. I. The Superhydrophobicity of Polymer Surfaces: Recent Developments. *J. Polym. Sci., Part B: Polym. Phys.* **2011**, *49*, 1203−1217.
(21) Guo, P.; Zheng, Y.; Wen, M.; Song, C.; Lin, Y.; Jiang, L. Icephobic/Anti-Icing Properties of Micro/Nanostructured Surfaces. *Adv. Mater.* **2012**, *24*, 2642−2648.
(22) Choi., M.-C.; Kim., Y.; Ha., C.-S. Polymers for Flexible Displays: From Material Selection to Device Applications. *Prog. Polym. Sci.* **2008**, *33*, 581−630.
(23) Chen, X.; Ma, R.; Zhou, H.; Zhou, X.; Che, L.; Yao, S.; Wang, Z. Activating the Microscale Edge Effect in a Hierarchical Surface for Frosting Suppression and Defrosting Promotion. *Sci. Rep.* **2013**, *3*, 2515-1−2515-8.
(24) Chen, C.-H.; Cai, Q.; Tsai, C.; Chen, C.-L.; Xiong, G.; Yu, Y.; Ren, Z. Dropwise Condensation on Superhydrophobic Surfaces with Two-Tier Roughness. *Appl. Phys. Lett.* **2007**, *90*, 173108-1−173108-3.
(25) Greene, L. E.; Law, M.; Tan, D. H.; Montano, M.; Goldberger, J.; Somorjai, G.; Yang, P. General Route to Vertical ZnO Nanowire Arrays Using Textured ZnO Seeds. *Nano Lett.* **2005**, *5*, 1231−1236.
(26) Vayssieres, L. Growth of Arrayed Nanorods and Nanowires of ZnO from Aqueous Solutions. *Adv. Mater.* **2003**, *15*, 464−466.
(27) Cui, J. B.; Daghlian, C. P.; Gibson, U. J.; Pusche, R.; Geithner, P.; Ley, L. Comparison of the Device Physics Principles of Planar and Radial p-n Junction Nanorod Solar Cells. *J. Appl. Phys.* **2005**, *97*, 044315−044317.
(28) He, J. H.; Hsu, J. H.; Wang, C. W.; Lin, H. N.; Chen, L. J.; Wang, Z. L. Pattern and Feature Designed Growth of ZnO Nanowire Arrays for Vertical Devices. *J. Phys.Chem. B.* **2006**, *110*, 50−53.
(29) Tian, D.; Zhang, X.; Wang, X.; Zhai, J.; Jiang, L. Micro/Nanoscale Hierarchical Structured ZnO Mesh Film for Separation of Water and Oil. *Phys. Chem. Chem. Phys.* **2011**, *13*, 14606−14610.
(30) Tian, D.; Chen, Q.; Nie, F.-Q.; Xu, J.; Song, Y.; Jiang, L. Patterned Wettability Transition by Photoelectric Cooperative and Anisotropic Wetting for Liquid Reprography. *Adv. Mater.* **2009**, *21*, 3744−3749.
(31) Kim, P.; Wong, T.-S.; Alvarenga, J.; Kreder, M. J.; Adorno-Martinez, W. E.; Aizenberg, J. Liquid-Infused Nanostructured Surfaces with Extreme Anti-Ice and Anti-Frost Performance. *ACS Nano* **2012**, *6*, 6569−6577.
(32) Chen, X.; Wu, J.; Ma, R.; Hua, M.; Koratkar, N.; Yao, S.; Wang, Z. Nanograssed Micropyramidal Architectures for Continuous Dropwise Condensation. *Adv. Funct. Mater.* **2011**, *21*, 4617−4623.
(33) Leese, H.; Bhurtun, V.; Lee, K. P.; Mattia, D. Wetting Behaviour of Hydrophilic and Hydrophobic Nanostructured Porous Anodic Alumina. *Colloids Surf., A* **2013**, *420*, 53−58.
(34) Wenzel, R. N. Surface Roughness and Contact Angle. *J. Phys. Colloid Chem.* **1949**, *53*, 1466−1467.